Author Manuscript

Author Manuscript

Author Manuscript

Author Manuscript

HHS Public Access

Author manuscript

J Fluid Mech. Author manuscript; available in PMC 2022 November 04.

Published in final edited form as:

J Fluid Mech. 2022 May 25; 939: . doi:10.1017/jfm.2022.215.

A one-dimensional model for the pulsating flow of cerebrospinal fluid in the spinal canal

S. Sincomb[1], **W. Coenen**[2], **C. Gutiérrez-Montes**[3], **C. Martínez Bazán**[4], **V. Haughton**[5], **A.L. Sánchez**[1,†]

[1]Department of Mechanical and Aerospace Engineering, UC San Diego, La Jolla, CA 92093-0411, USA

[2]Grupo de Mecánica de Fluidos, Universidad Carlos III de Madrid, Leganés (Madrid) 28911, Spain

[3]Grupo de Mecánica de Fluidos, Universidad de Jaén, Jaén 23071, Spain

[4]Grupo de Mecánica de Fluidos, Universidad de Granada, Granada 18071, Spain

[5]Department of Radiology, University of Wisconsin-Madison, Madison, WI 53792-3252, USA

Abstract

The monitoring of intracranial pressure (ICP) fluctuations, which is needed in the context of a number of neurological diseases, requires the insertion of pressure sensors, an invasive procedure with considerable risk factors. Intracranial pressure fluctuations drive the wave-like pulsatile motion of cerebrospinal fluid (CSF) along the compliant spinal canal. Systematically derived simplified models relating the ICP fluctuations with the resulting CSF flow rate can be useful in enabling indirect evaluations of the former from non-invasive magnetic resonance imaging (MRI) measurements of the latter. As a preliminary step in enabling these predictive efforts, a model is developed here for the pulsating viscous motion of CSF in the spinal canal, assumed to be a linearly elastic compliant tube of slowly varying section, with a Darcy pressure-loss term included to model the fluid resistance introduced by the *trabeculae,* which are thin collagen-reinforced columns that form a web-like structure stretching across the spinal canal. Use of Fourier-series expansions enables predictions of CSF flow rate for realistic anharmonic ICP fluctuations. The flow rate predicted using a representative ICP waveform together with a realistic canal anatomy is seen to compare favourably with *in vivo* phase-contrast MRI measurements at multiple sections along the spinal canal. The results indicate that the proposed model, involving a limited number of parameters, can serve as a basis for future quantitative analyses targeting predictions of ICP temporal fluctuations based on MRI measurements of spinal-canal anatomy and CSF flow rate.

Keywords

biological fluid dynamics

[†]Email address for correspondence: als@ucsd.edu.

Declaration of interests. The authors report no conflict of interest.

Author Manuscript Author Manuscript Author Manuscript Author Manuscript

1. Introduction

The cerebrospinal fluid (CSF) is a clear fluid that fills the ventricles of the brain as well as the subarachnoid spaces (SSASs) (Linninger et al. 2016). Normal CSF behaves as a Newtonian fluid (Ommaya 1968; Bloomfield, Johnston & Bilston 1998) and its properties are very close to those of water (i.e. density $\rho = 10^3$ kg m^{-3} and kinematic viscosity $\nu = 0.7 \times 10^{-6}$ m^2 s^{-1}). The motion of CSF in the central nervous system, which has important physiological functions and plays a role in the development of different neurological diseases, has been the subject of numerous studies, as reviewed by Linninger et al. (2016). Recent efforts include numerical simulations of the entire cranial cavity (Gholampour & Fatouraee 2021) and investigations of flow in the perivascular spaces of cerebral arteries (Thomas 2019; Carr et al. 2021; Coenen, Zhang & Sánchez 2021) and along the cerebral aqueduct (Sincomb et al. 2020, 2021), for example. The present paper deals with the motion along the SSAS, a slender compliant canal of length $L \simeq 60$ cm bounded internally by the *pia mater* surrounding the spinal cord and externally by the deformable *dura* membrane (see figure 1a). The arterial blood flow in and out of the rigid cranial vault causes the intracranial pressure (ICP) to fluctuate in time following the cardiac cycle (Du Boulay 1966; Bhadelia et al. 1997; Wagshul et al. 2006), driving the pulsatile motion of CSF along the SSAS.

Continuous ICP monitoring is key in the assessment of surgical intervention and also for guiding therapy for cases of traumatic brain injury (TBI), normal pressure hydrocephalus (NPH) and other neurointensive states. Although the mean ICP value is often used clinically, it is of interest to also assess the pulsatile ICP variation or morphology. As shown in figure 1(b), the ICP waveform generally has three peaks associated with the cardiac cycle whose amplitudes decrease in a stepwise manner in a healthy individual (Singh & Cheng 2021). The waveform is altered due to the changes in intracranial volume (Unnerbäck, Ottesen & Reinstrup 2018), an important result in the context of disease conditions that produce an increase in mean ICP (TBI or *oedema* formation), which can result in the waveform becoming more rounded (Ellis, McNames & Aboy 2007), or NPH, which leads to greater fluctuation amplitudes (Eide & Sorteberg 2016). The insertion of ICP sensors requires a burr hole made into the skull. Since the procedure has inherent risks, including haemorrhage and infection (Evensen & Eide 2020), there is interest in developing non-invasive techniques for ICP characterization. The approach postulated here exploits the close connection existing between the ICP waveform and the resulting CSF motion along the spinal canal. It is reasoned that detailed knowledge of the flow rate along the canal, obtained via phase-contrast magnetic resonance imaging (PC-MRI) techniques (Feinberg & Mark 1987), can be used to infer the associated ICP waveform.

The flow in the canal fundamentally involves a fluid–structure interaction problem, which depends on detailed anatomical features of the canal determining its compliance and flow resistance (Linninger et al. 2016). As summarized by Khani et al. (2018), most previous modelling efforts are based on numerical simulations with different levels of complexity. Analytic flow models involving a reduced number of parameters can be more useful in enabling inverse predictions of ICP from measurements of flow rates. One-dimensional models for pressure/flow wave propagation along the spinal canal have been developed in the past using a coaxial cylindrical tube configuration (Berkouk, Carpenter & Lucey 2003;

Author Manuscript Author Manuscript Author Manuscript Author Manuscript

Carpenter, Berkouk & Lucey 2003; Cirovic & Kim 2012). More elaborate three-dimensional flow models assuming a thin annular canal of non-uniform width are also available (Sánchez et al. 2018; Lawrence et al. 2019; Gutiérrez-Montes et al. 2021). These previous efforts have assumed the canal section to be open, thereby neglecting the pressure loss introduced by spinal microstructures, effects of which have been quantified numerically by Tangen et al. (2015). Their analysis showed that most of the increase in pressure loss is associated with the *arachnoid trabeculae,* which are thin collagen-reinforced columns that form a web-like structure stretching across the SSAS (Mortazavi et al. 2018). Following Gupta et al. (2009), our analysis will model the complex *trabeculae* network as a porous medium of variable permeability. For increased generality, no specific shape will be assumed for the canal cross-section, thereby generalizing our previous analyses (Sánchez et al. 2018; Lawrence et al. 2019; Gutiérrez-Montes et al. 2021), postulating the SSAS to be a thin annular canal surrounding the spinal cord, an assumption that necessarily fails in the *sacral* region, as shown in the cross-sectional views of figure 1(a).

2. Preliminary considerations

2.1. The ICP

Attention will be focused on the motion induced by the cardiac cycle, associated with the periodic temporal fluctuations of the ICP $p_c(t)$ from its mean value $\langle p_c \rangle = T^{-1}\int_t^{t+T} p_c \, \mathrm{d}t$, where $T \simeq 1\mathrm{s}$ is the period of the cardiac cycle. These fluctuations can in general be represented in the form $p_c(t) - \langle p_c \rangle = \Delta p \Pi(\omega t)$, involving the mean fluctuation amplitude $\Delta p = T^{-1}\int_t^{t+T} | p_c - \langle p_c \rangle | \, \mathrm{d}t$, which typically takes values of the order of $\Delta p \sim 50$–100 Pa, along with a dimensionless function $\Pi(\omega t)$ describing the waveform, with $\omega = 2\pi/T$ denoting the relevant angular frequency. Note that the function Π must satisfy $\int_t^{t+T} \Pi \, \mathrm{d}t = 0$ and $T^{-1}\int_t^{t+T} | \Pi | \, \mathrm{d}t = 1$, for consistency with the definition of Δp.

2.2. The canal geometry

In deriving a simple one-dimensional model for the flow dynamics, the spinal canal will be modelled as a tube displaying a slowly varying shape over its length $L \simeq 50$–70 cm. The flow is to be described in terms of curvilinear coordinates (x, y, z), with the streamwise distance x measured from the open end, connected to the cranial cavity through the *foramen magnum,* with the closed *sacral* end corresponding to $x = L$, as indicated in figure 1(a). As seen in figure 1(a), in the stretch of canal occupied by the spinal cord the cross-sectional shape is an annulus, bounded internally by the *pia mater* and externally by the *dura mater.* In the one-dimensional model developed below the morphology of the cross-section enters only through two related quantities that vary along the spinal canal, namely, the cross-sectional area occupied by CSF at each transverse section $A(x)$ and the length of the wetted boundary $\ell(x)$, the latter including the *pia mater* surrounding the spinal cord. The average cross-sectional area is given by $A_o = V_{CSF}/L \simeq 1.5\ \mathrm{cm}^2$, where $V_{CSF} = \int_0^L A \, \mathrm{d}x \simeq 80\ \mathrm{cm}^3$ is the total volume of CSF in the in the SSAS (Edsbagge et al. 2011). Since the characteristic transverse length $A_o^{1/2}$ satisfies $A_o^{1/2} \ll L$, the flow is fundamentally slender. Fluid motion predominantly occurs in the axial direction, with streamwise velocity $u(x, y, z, t)$ driven by

Author Manuscript Author Manuscript Author Manuscript Author Manuscript

the streamwise pressure distribution $p(x, t)$ (Sánchez et al. 2018), assumed to be uniform across the canal section, as is consistent with the slender-flow approximation.

2.3. Governing equations

During each cardiac cycle, the ICP pulsation drives a small volume $\Delta V \sim 1\ \mathrm{cm}^3$ of CSF in and out of the spinal canal (Linninger et al. 2016). This oscillating flow is accommodated by the displacement of fat tissue and *venous* blood, which results in a periodic change ΔA of the local cross-sectional area A at a given location. Since the characteristic stroke volume ΔV is much smaller than the total CSF volume V_{CSF}, these temporal changes are small, i.e. $\Delta A \sim (\Delta V/V_{CSF})A_o \sim 1\ \mathrm{mm}^2$. To model these changes, we shall adopt the linear elastic model,

$$\frac{\partial A}{\partial t} = \gamma \frac{\partial p}{\partial t}, \tag{2.1}$$

involving a local compliance $\gamma(x)$ having dimensions of surface over pressure with mean value $\gamma_o = L^{-1}\int_0^L \gamma(x)\,\mathrm{d}x$.

To maximize the simplicity and facilitate comparisons with *in vivo* results, CSF motion is to be characterized with use of the local volumetric flow rate $Q(x, t) = \int\int u\,\mathrm{d}y\,\mathrm{d}z$, obtained by integrating the streamwise velocity $u(x, y, z, t)$ across the canal section. Its streamwise variation is related with the temporal variation of the cross-sectional area through the integrated continuity equation $\partial Q/\partial x + \partial A/\partial t = 0$, which can be rewritten in the form

$$\frac{\partial Q}{\partial x} + \gamma(x)\frac{\partial p}{\partial t} = 0, \tag{2.2}$$

after substitution of (2.1). On the other hand, the axial component of the momentum balance equation can be simplified by neglecting convective acceleration, whose magnitude can be shown to be a factor $\Delta V/V_{CSF}$ smaller than that of the local acceleration (Sánchez et al. 2018), along with the contribution of streamwise derivatives to the viscous force. Furthermore, following Gupta et al. (2009), the pressure loss caused by the *trabeculae* network is modelled using Darcy's law, yielding (Kurtcuoglu, Jain & Martin 2019)

$$\frac{\partial u}{\partial t} = -\frac{1}{\rho}\frac{\partial p}{\partial x} + \nu\left(\frac{\partial^2 u}{\partial y^2} + \frac{\partial^2 u}{\partial z^2}\right) - \frac{\nu}{\kappa}u, \tag{2.3}$$

where $\kappa(x)$ is the SSAS permeability, whose value depends on the number and structure of the *arachnoid trabeculae.*

2.4. The inviscid wave model

It is illustrative to consider first the inviscid case $\nu = 0$, for which integration of (2.3) across the canal yields

$$\frac{\partial Q}{\partial t} + \frac{A(x)}{\rho}\frac{\partial p}{\partial x} = 0\,. \tag{2.4}$$

Author Manuscript Author Manuscript Author Manuscript Author Manuscript

In writing the above equation, we have neglected the small temporal variation of the cross-sectional area A, as is consistent with the condition $\Delta A \ll A_o$ previously discussed. Equations (2.2) and (2.4) can be integrated with boundary conditions $p = p_c$ at $x = 0$ and $Q = 0$ at $x = L$ to determine the periodic variation of the pressure and flow rate along the canal. The wave nature of the flow can be emphasized by considering a canal with constant section $A(x) = A_o$ and constant compliance $\gamma(x) = \gamma_o$, for which (2.2) and (2.4) can be combined to give

$$\frac{\partial^2 p}{\partial t^2} = c^2 \frac{\partial^2 p}{\partial x^2} \text{ and } \frac{\partial^2 Q}{\partial t^2} = c^2 \frac{\partial^2 Q}{\partial x^2}, \tag{2.5}$$

where

$$c = \left(\frac{A_o}{\rho \gamma_o}\right)^{1/2} \tag{2.6}$$

is the elastic wave speed of the problem (Grotberg & Jensen 2004). For a harmonic ICP fluctuation $p_c - (p_c) = \Delta p(\pi/2) \cos(\omega t)$, the above wave equation can be solved to give

$$Q = -\frac{\pi}{2} \gamma_o L \omega \Delta p \sin(\omega t) \frac{\sin[k(1 - x/L)]}{k \cos k}, \tag{2.7}$$

where

$$k = \frac{L\omega}{c} = \left(\frac{\rho \gamma_o L^2 \omega^2}{A_o}\right)^{1/2} \tag{2.8}$$

is a relevant dimensionless wavenumber. The flow rate (2.7) oscillates in phase along the entire canal, that being a fundamental limitation of the inviscid model, which is unable to reproduce the streamwise phase lag of the flow rate that has been consistently observed in MRI measurements (Yallapragada & Alperin 2004; Wagshul et al. 2006; Tangen et al. 2015). As shown below, consideration of viscous pressure losses, including those associated with the *trabeculae,* is needed to describe both the phase lag and the rate of streamwise attenuation of the flow rate.

3. A dimensionless flow model accounting for flow resistance

To reduce the parametric dependence, it is convenient to formulate the problem in dimensionless form using ω^{-1}, L and $A_o^{1/2}$ as scales for the time and for the longitudinal and transverse length scales, respectively. In looking for appropriate scales for Q and p, one may note from (2.2) that the characteristic value Q_c of the volume flux associated with an ICP fluctuation of magnitude Δp is $Q_c = \gamma_o \omega L \Delta p$, and from (2.4) that the corresponding streamwise variations of the pressure are of order $p - p_c \sim k^2 \Delta p$, with k denoting the wavenumber defined in (2.8). These scales lead to the new variables

Author Manuscript Author Manuscript Author Manuscript Author Manuscript

$$\left.\begin{aligned} \tau = \omega t,\ \ \xi = \frac{x}{L},\ \ \hat{y} = \frac{y}{A_o^{1/2}},\ \ \hat{z} = \frac{z}{A_o^{1/2}}, \\ \hat{u} = \frac{u}{Q_c / A_o},\ \ \hat{Q} = \frac{Q}{Q_c},\ \ \hat{p} = \frac{p - p_c}{k^2 \Delta p}. \end{aligned}\right\} \tag{3.1}$$

Similarly, A_o and γ_o are used to define the functions $\hat{A} = A / A_o$ and $\hat{\gamma} = \gamma / \gamma_o$.

The development begins by writing the continuity equation (2.2) in the reduced form

$$\frac{\partial \hat{Q}}{\partial \xi} + \hat{\gamma}\left(\frac{\mathrm{d}\Pi}{\mathrm{d}\tau} + k^2 \frac{\partial \hat{p}}{\partial \tau}\right) = 0\,. \tag{3.2}$$

With the scales selected, the momentum equation (2.3) takes the dimensionless form

$$\frac{\partial \hat{u}}{\partial \tau} = -\frac{\partial \hat{p}}{\partial \xi} + \frac{1}{\alpha^2}\left(\frac{\partial^2 \hat{u}}{\partial \hat{y}^2} + \frac{\partial^2 \hat{u}}{\partial \hat{z}^2}\right) - \mathscr{R}(\xi)\hat{u}, \tag{3.3}$$

where $\alpha = (A_o \omega / \nu)^{1/2}$ is the relevant Womersley number and $\mathscr{R}(\xi) = \nu / (\kappa\omega)$ is a dimensionless resistance coefficient. The velocity must satisfy the no-slip condition $\hat{u} = 0$ on the canal boundary Σ. Integrating the above equation across the canal section yields

$$\frac{\partial \hat{Q}}{\partial \tau} + \hat{A}(\xi)\frac{\partial \hat{p}}{\partial \xi} = -\frac{1}{\alpha^2}\int_{\Sigma} \hat{\tau}_f \,\mathrm{d}s - \mathscr{R}(\xi)\hat{Q}, \tag{3.4}$$

where $\mathrm{d}s$ the element of arclength measured at a given section along the canal boundary Σ and $\hat{\tau}_f = \partial \hat{u} / \partial n$ is the dimensionless viscous stress at $n = 0$, where n denotes the dimensionless distance from the wall.

3.1. Simplifications for $\alpha \gg 1$

The solution can be simplified by taking into account that the characteristic viscous time across the canal section A_o/ν is fairly large compared with the characteristic pulsation time ω^{-1}. In the associated limit $\alpha \gg 1$, the longitudinal velocity is uniform outside a thin near-wall Stokes layer of rescaled thickness $\alpha^{-1} \ll$C 1. The uniform velocity in the inviscid core varies along the canal according to $\hat{u} = \hat{Q}(\xi, \tau) / \hat{A}(\xi)$, while the accompanying pressure gradient is $\partial \hat{p} / \partial \xi = -(\partial \hat{Q} / \partial \tau + \mathscr{R}\hat{Q}) / \hat{A}$. Viscous forces are important in the Stokes layer, across which the velocity $\hat{u}_S$ evolves from the inviscid value $\hat{Q} / \hat{A}$ to a zero value at $n = 0$, as described by the reduced problem

$$\frac{\partial \hat{u}_S}{\partial \tau} - \frac{1}{\hat{A}(\xi)}\frac{\partial \hat{Q}}{\partial \tau} = \frac{\partial^2 \hat{u}_S}{\partial \eta^2} + \mathscr{R}(\xi)\left(\frac{\hat{Q}}{\hat{A}(\xi)} - \hat{u}_S\right)\begin{cases} \eta = 0: & \hat{u}_S = 0 \\ \eta \to \infty: & \hat{u}_S \to \hat{Q} / \hat{A} \end{cases}, \tag{3.5}$$

where $\eta = \alpha n$. The solution to (3.5) determines in particular the value of $\hat{u}'_o(\xi, \tau) = \partial \hat{u}_S / \partial \eta\,|_{\eta = 0}$, which can be used to write (3.4) in the form

Author Manuscript Author Manuscript Author Manuscript Author Manuscript

$$\frac{\partial \widehat{Q}}{\partial \tau} + \widehat{A}(\xi)\frac{\partial \widehat{p}}{\partial \xi} = -\frac{\widehat{\ell}(\xi)}{\alpha}\widehat{u}_o' - \mathscr{R}(\xi)\widehat{Q}\,. \tag{3.6}$$

As expected, since at leading order in the limit $\alpha \gg 1$ the structure of the Stokes layer is identical all around the canal wall, the term $-\widehat{\ell}\widehat{u}_o'/\alpha$ representing in (3.6) the viscous force $-\int_\Sigma \widehat{\tau}_f \,\mathrm{d}s/\alpha^2$ is linearly proportional to the dimensionless length of the wetted boundary $\widehat{\ell}(\xi) = \ell/A_o^{1/2}$.

3.2. Solution in terms of Fourier expansions

The problem can be solved for a given general periodic function $\Pi(\tau) = \sum_{n=1}^{\infty} \mathrm{Re}(B_n \mathrm{e}^{\mathrm{i}n\tau})$, where Re indicates the real part, i is the imaginary unit, and B_n are complex constants, by introducing accompanying Fourier expansions

$$\left.\begin{aligned} \widehat{p} &= \sum_{n=1}^{\infty} \mathrm{Re}(B_n P_n(\xi)\,\mathrm{e}^{\mathrm{i}n\tau}), \\ \widehat{Q} &= \sum_{n=1}^{\infty} \mathrm{Re}(B_n \mathrm{i}n Q_n(\xi)\,\mathrm{e}^{\mathrm{i}n\tau}), \\ \widehat{u}_S &= \frac{1}{\widehat{A}(\xi)}\sum_{n=1}^{\infty} \mathrm{Re}(B_n \mathrm{i}n Q_n(\xi) f_n(\eta)\,\mathrm{e}^{\mathrm{i}n\tau}), \end{aligned}\right\} \tag{3.7}$$

for the pressure, volume flow rate and Stokes-layer velocity, with $P_n(\xi)$, $Q_n(\xi)$ and $f_n(\eta)$ representing complex functions. The function $f_n = 1 - \exp[-(\mathrm{i}n + \mathscr{R})^{1/2}\eta]$ is obtained from the reduced Stokes problem

$$(\mathrm{i}n + \mathscr{R})(f_n - 1) = \frac{\mathrm{d}^2 f_n}{\mathrm{d}\eta^2}\begin{cases} \eta = 0: & f_n = 0 \\ \eta \to \infty: & f_n \to 1 \end{cases}, \tag{3.8}$$

which follows from introduction of (3.7) into (3.5), thereby yielding $\mathrm{d}f_n/\mathrm{d}\eta(0) = (\mathrm{i}\,n + \mathscr{R})^{1/2}$ and

$$\widehat{u}_o' = \frac{1}{\widehat{A}(\xi)}\sum_{n=1}^{\infty} \mathrm{Re}[B_n \mathrm{i}n Q_n(\xi)[\mathrm{i}n + \mathscr{R}(\xi)]^{1/2}\,\mathrm{e}^{\mathrm{i}n\tau}]\,. \tag{3.9}$$

Substituting (3.7) and (3.9) into (3.2) and (3.6) leads to the first-order linear ordinary differential equations

$$\frac{\mathrm{d}Q_n}{\mathrm{d}\xi} + \hat{\gamma}(\xi)[1 + k^2 P_n] = 0, \tag{3.10}$$

Author Manuscript Author Manuscript Author Manuscript Author Manuscript

$$\widehat{A}(\xi)\frac{\mathrm{d}P_n}{\mathrm{d}\xi} = \left\{n^2 - \mathrm{i}n\left[\frac{\widehat{\ell}(\xi)}{\alpha\widehat{A}(\xi)}[\mathrm{i}n + \mathscr{R}(\xi)]^{1/2} + \mathscr{R}(\xi)\right]\right\}Q_n, \tag{3.11}$$

which can be further combined to generate the boundary-value problem

$$\left.\begin{aligned}\frac{\mathrm{d}}{\mathrm{d}\xi}\left[\frac{1}{\widehat{\gamma}(\xi)}\frac{\mathrm{d}Q_n}{\mathrm{d}\xi}\right] + \frac{k^2}{\widehat{A}(\xi)}\left\{n^2 - \mathrm{i}n\left[\frac{\widehat{\ell}(\xi)}{\alpha\widehat{A}(\xi)}[\mathrm{i}n + \mathscr{R}(\xi)]^{1/2} + \mathscr{R}(\xi)\right]\right\}Q_n = 0,\\ \frac{\mathrm{d}Q_n}{\mathrm{d}\xi}(0) + \widehat{\gamma}(0) = Q_n(1) = 0,\end{aligned}\right\} \tag{3.12}$$

for $Q_n(\xi)$, with the value of $\mathrm{d}Q_n/\mathrm{d}\xi$ at $\xi = 0$ following from using $P_n(0) = 0$ in (3.10).

It is worth noting that the terms in the large square brackets in (3.11) represent the pressure losses associated with the Stokes layer developing on the canal boundary (the term proportional to $[\mathrm{i}n + \mathscr{R}]^{1/2}$) and with the *trabeculae* (the term proportional to $\mathscr{R}$). The two pressure losses have different phase, so that they have distinct effects on the resulting flow rate, as can be inferred from (3.12). Since the resistance exerted by the Stokes layer is inversely proportional to α, it tends to have a lesser effect, especially on the first Fourier mode $n = 1$, for which the pressure loss associated with the *trabeculae* is significantly higher. Although simplified flow descriptions neglecting the presence of the Stokes layer are worth exploring in future work, for completeness the computations presented below utilize the full equation (3.12) in evaluating the flow rate.

For a canal of uniform section, uniform compliance and uniform permeability (i.e. $\widehat{A} = \widehat{\gamma} = 1$, $\widehat{\ell}$ = constant and $\mathscr{R}$ = constant) the solution reduces to Q_n - $\sin[\beta_n(1 - \xi)]/(\beta_n \cos\beta_n)$, with

$$\beta_n = kn\left\{1 + \left[\frac{1 - \mathrm{i}}{(\alpha/\widehat{\ell})\sqrt{2n}}\left(1 - \frac{\mathscr{R}\mathrm{i}}{n}\right)^{1/2} - \frac{\mathscr{R}\mathrm{i}}{n}\right]\right\}^{1/2}. \tag{3.13}$$

It is worth noting that the inviscid limit considered earlier corresponds to $\beta_n = kn$, the limiting form of (3.13) for $\alpha \gg 1$ and $\mathscr{R} = 0$. For the case $B_1 = \pi/2$ and $B_n = 0$ for $n > 1$, associated with the harmonic ICP $p_c = \Delta p\,(\pi/2)\cos(\omega t)$, the Fourier series for the flow rate reduces to the single term

$$\widehat{Q} = \mathrm{Re}\left(\frac{\pi}{2}\,\mathrm{i}\,\frac{\sin[k(1 - \xi)]}{k\cos k}\,\mathrm{e}^{\mathrm{i}\tau}\right) = -\frac{\pi}{2}\sin\tau\,\frac{\sin[k(1 - \xi)]}{k\cos k}, \tag{3.14}$$

consistent with (2.7).

4. Illustrative sample applications

In general, numerical integration of (3.12) is needed to determine $Q_n(\xi)$. The solution depends on the anatomical characteristics of the SSAS, including its length L, average cross-sectional area A_o and geometric functions $\widehat{A} = A/A_o$ and $\widehat{\ell} = \ell/A_o^{1/2}$. For a given subject,

Author Manuscript Author Manuscript Author Manuscript Author Manuscript

the necessary anatomical data can be determined from high-resolution MRI images, as explained for instance in Coenen et al. (2019). The computations reported below correspond to two subjects: a healthy 27-year-old female with $L = 60$ cm, $A_o = 182$ mm^2 and $\alpha = (A_o\omega/\nu)^{1/2} = 40$ (subject 1); and a healthy 39-year-old male with $L = 64$ cm, $A_o = 138$ mm^2 and $\alpha = 35$ (subject 2), both with cardiac period $T = 2\pi/\omega = 1$ s. The functions $\hat{A}(\xi)$ and $\hat{\ell}(\xi)$ shown in figure 1(b) are obtained by the boundaries of the binary image stack resulting from segmentation of the high resolution MRI images.

The value of $\mathscr{R} = \nu / (\kappa\omega)$ depends on the permeability κ, which in turn is a function of the SSAS porosity ϵ and *trabeculae* transverse size. In the following, we shall assume that κ, is uniform and adopt the approximate formula $\kappa = \pi a^2 \epsilon (1 - \sqrt{1-\epsilon})^2 / [24(1-\epsilon)^{3/2}]$, derived by Gupta et al. (2009) for a *trabeculae* network comprising cylindrical posts of radius a extending normally to the *arachnoid* layer. For a porosity $\epsilon = 0.99$, a value estimated by Tada & Nagashima (1994), and a *trabeculae* radius $a = 15$ μm (Stockman 2006) this approximate formula gives $\kappa = 2.362 \times 10^{-8}$ m^2, corresponding to a dimensionless resistance factor $\mathscr{R} = 4.78$, to be used below.

Limited information is available on the spinal canal compliance γ (Tangen et al. 2015). Although departures of γ from its mean value γ_o can be expected as a result of the unequal distribution of fat tissue and epidural veins along the canal, possibly resulting in a smaller value of γ in the cervical region (Yallapragada & Alperin 2004), a uniform value $\gamma = \gamma_o$ is to be employed in the following sample computation, for which $\hat{\gamma} = \gamma / \gamma_o = 1$. To estimate the average compliance γ_o, which determines from (2.8) the dimensionless wavenumber k, one may use (2.6) to relate γ_o with the elastic wave speed c. Using the value $c = 4.6$ m s^{-1} reported by Kalata et al. (2009) for healthy humans, it follows from (2.6) that $\gamma_0 = 8.6 \times 10^{-9}$ m^2 Pa^{-1} and from (2.8) that $k \simeq 0.81$ for subject 1, with corresponding values $\gamma_0 = 6.5 \times 10^{-9}$ m^2 Pa^{-1} and $k \simeq 0.86$ for subject 2.

The modes $\hat{Q}_n$ determined from (3.12) with use made of the anatomical values reported above were used in (3.7) to compute the corresponding dimensionless flow rate $\hat{Q}$ yielding the results shown in figures 2(c) and 3(c). The computation of $\hat{Q}$ involves 10 Fourier coefficients B_n, corresponding to the function $\Pi(\tau)$ shown in figure 1(b), taken as representative of a healthy state ICP waveform (Di Ieva, Schmitz & Cusimano 2013). The results are compared in figures 2 and 3 with flow rate measurements acquired at 12 vertebral levels using PC-MRI with retrospective cardiac gating in *in vivo* experiments involving the two subjects (see Coenen et al. (2019) for details of the data-acquisition process). To establish a quantitatively consistent comparison, the results are presented in normalized form. Thus, the stroke volume $V_S(\xi) = \frac{1}{2}\int_t^{t+T} |Q| \, dt$ measured via MRI is scaled with its entrance value (i.e. $V_S(0) = 0.7$ cm^3 for subject 1 and $V_S(0) = 0.6$ cm^3 for subject 2), while the model prediction $\hat{V}_S(\xi) = \frac{1}{2}\int_\tau^{\tau+2\pi} |\hat{Q}| \, d\tau$ is correspondingly scaled with $\hat{V}_S(0)$, with $\hat{V}_S(0) = 1.9$ for subject 1 and $\hat{V}_S(0) = 1.8$ for subject 2. Similarly, the PC-MRI flow rate measurements are scaled with its characteristic value $\omega V_S(0)$ while the predicted flow rate $\hat{Q}$ is scaled with $\hat{V}_S(0)$.

Author Manuscript Author Manuscript Author Manuscript Author Manuscript

With the uniform values $\hat{\gamma} = 1$ and $\mathscr{R} = 4.78$ selected in the computations, the comparisons in figures 2 and 3 indicate that the model is able to describe reasonably well the main features of the pulsating flow rate, including its particular shape and the phase lag of its peak value. In addition, the streamwise decay of the stroke volume (figures 2g and 3g*),* a metric often used in the medical community to characterize CSF flow, is seen to agree well with the corresponding values computed from the MRI data, with root-mean-square differences between model and MRI remaining below 0.09 for both subjects. As a further consistency check, one may use the measured value of $V_S(0)$ along with the accompanying dimensionless prediction $\hat{V}_S(0)$ to obtain from the definition $V_S(0) = \gamma_o L \Delta p \hat{V}_S(0)$ an estimate for the mean fluctuation amplitude Δp. The value obtained, $\Delta p = 73$ Pa for subject 1 and $\Delta p = 80$ Pa for subject 2, corresponding to a peak-to-peak value of approximately 200 Pa, is well within the range of values reported in the literature (Eide & Brean 2006), thereby providing additional confidence in the model.

To investigate the sensitivity of the model predictions to changes in *trabeculae* resistance, results for varying $\mathscr{R}$ are also included in figures 2 and 3. In the absence of *trabeculae,* i.e. for $\mathscr{R} = 0$, both the rate at which the flow rate fluctuation decays along the canal and the general flow rate waveform, including the associated phase lag, are in poor agreement with the MRI measurements. Consequently, for $\mathscr{R} = 0$ the modelled streamwise decay of stroke volume, shown in figures 2(g) and 3(g), is also seen to strongly overpredict the amount of CSF flow in the thoracic and lumbar regions compared with the MRI measurements. These quantitative findings emphasize the important effects of *trabeculae,* previously pointed out by Tangen et al. (2015). As can be seen in figures 2 and 3, the results are not very sensitive to the specific choice of $\mathscr{R}$, provided that an order-unity value is selected. Nevertheless, the computations obtained with $\mathscr{R} = 4.78$, the value determined using the permeability and other anatomical features taken from the literature (Tada & Nagashima 1994; Stockman 2006; Gupta et al. 2009), appear to give better overall agreement with the MRI measurements, providing the optimal amount of attenuation all along the canal.

5. Concluding remarks

The temporal and spatial variation of the flow rate predicted by the one-dimensional model developed here supplemented with a presumed ICP waveform has been shown to predict the main features revealed in *in vivo* experiments. Utilization of the model in future efforts to develop non-invasive measurements of ICP requires the solution of the inverse problem, i.e. the computation of the ICP fluctuation from the PC-MRI flow measurements. Given the uncertainty regarding the canal compliance and the *trabeculae*-network properties, it is unclear whether conventional parameter-fitting approaches will be successful in these future developments or whether more elaborate optimization algorithms, possibly based on machine-learning techniques, will be needed. In improving the model, these future efforts should also account for localized pressure losses associated with the presence of additional spinal microstructures, such as nerve roots and ligaments.

Author Manuscript Author Manuscript Author Manuscript Author Manuscript

Funding.

The work of S.C., V.H. and A.L.S. was supported by the National Institute of Neurological Disorders and Stroke through contract no. 1R01NS120343-01. The work of W.C. was supported by the Comunidad de Madrid through the contract CSFFLOW-CM-UC3M. C.M.B., C.G. and W.C. acknowledge the support of the Spanish MICINN through the coordinated project PID2020-115961RB. C.M.B. and C.G. also acknowledge the support provided by Junta de Andalucía and European Funds through grant P18-FR-4619.

References

Berkouk K, Carpenter PW & Lucey AD 2003 Pressure wave propagation in fluid-filled co-axial elastic tubes part 1: basic theory. Trans. ASME J. Biomech. Engng 125 (6), 852–856.

Bhadelia RA, Bogdan AR, Kaplan RF & Wolpert SM 1997 Cerebrospinal fluid pulsation amplitude and its quantitative relationship to cerebral blood flow pulsations: a phase–contrast MR flow imaging study. Neuroradiology 39 (4), 258–264. [PubMed: 9144672]

Bloomfield IG, Johnston, IH & Bilston LE 1998 Effects of proteins, blood cells and glucose on the viscosity of cerebrospinal fluid. Pediatr. Neurosurg 28 (5), 246–251. [PubMed: 9732257]

Carpenter PW, Berkouk K & Lucey AD 2003 Pressure wave propagation in fluid-filled co-axial elastic tubes. Part 2: mechanisms for the pathogenesis of syringomyelia. Trans. ASME J. Biomech. Engng 125 (6), 857–863.

Carr JB. Thomas JH. Liu J & SHANG JK 2021 Peristaltic pumping in thin non-axisymmetric annular tubes. J. Fluid Mech 917, A10. [PubMed: 35310826]

Cirovic S & Kim M 2012 A one-dimensional model of the spinal cerebrospinal-fluid compartment. Trans. ASME J. Biomech. Engng 134 (2). 021005.

Coenen W, Gutiérrez-Montes C, Sincomb S, Criado-Hidalgo E, Wei K, King K, Haughton V, Martínez-Bazán C, Sánchez AL & Lasheras JC 2019 Subject-specific studies of CSF bulk flow patterns in the spinal canal: implications for the dispersion of solute particles in intrathecal drug delivery. Am. J. Neuroradiol 40, 1242–1249. [PubMed: 31196863]

Coenen W, Zhang X & Sánchez AL 2021 Lubrication analysis of peristaltic motion in non-axisymmetric annular tubes. J. Fluid Mech 921, R2.

Di Ieva A. Schmitz EM & Cusimano MD 2013 Analysis of intracranial pressure: past, present, and future. Neuroscientist 19 (6), 592–603. [PubMed: 23389057]

Du Boulay GH 1966 Pulsatile movements in the CSF pathways. Br. J. Radiol 39 (460), 255–262. [PubMed: 5295581]

Edsbagge M, Starck G, Zetterberg H, Ziegelitz D & Wikkelso C 2011 Spinal cerebrospinal fluid volume in healthy elderly individuals. Clin. Anat 24 (6), 733–740. [PubMed: 21412855]

Eide PK & Brean A 2006 Intracranial pulse pressure amplitude levels determined during preoperative assessment of subjects with possible idiopathic normal pressure hydrocephalus. Acta Neurochir. 148 (11). 1151–1156. [PubMed: 17039303]

Eide PK & Sorteberg W 2016 Outcome of surgery for idiopathic normal pressure hydrocephalus: role of preoperative static and pulsatile intracranial pressure. World Neurosurg. 86, 186–193. [PubMed: 26428326]

Ellis T, McNames J & Aboy M 2007 Pulse morphology visualization and analysis with applications in cardiovascular pressure signals. IEEE Trans. Biomed 54 (9), 1552–1559.

Evensen KB & Eide PK 2020 Measuring intracranial pressure by invasive, less invasive or non-invasive means: limitations and avenues for improvement. Fluids Barriers CNS 17 (1). 34. [PubMed: 32375853]

Feinberg DA & Mark AS 1987 Human brain motion and cerebrospinal fluid circulation demonstrated with MR velocity imaging. Radiology 163 (3), 793–799. [PubMed: 3575734]

Gholampour S & Fatouraee N 2021 Boundary conditions investigation to improve computer simulation of cerebrospinal fluid dynamics in hydrocephalus patients. Commun. Biol 4 (1), 394. [PubMed: 33758352]

Grotberg JB & Jensen OE 2004 Biofluid mechanics in flexible tubes. Annu. Rev. Fluid Mech 36, 121–147.

Author Manuscript Author Manuscript Author Manuscript Author Manuscript

Gupta S, Soellinger M, Boesiger P Poulikakos D & Kurtcuoglu V 2009 Three-dimensional computational modeling of subject-specific cerebrospinal fluid flow in the subarachnoid space. Trans. ASME J. Biomech. Engng 131 (2), 021010.

Gutiérrez-Montes C, Coenen W, Lawrence JJ. Martínez-Bazán C, Sánchez AL & Lasheras JC 2021 Modelling and direct numerical simulation of flow and solute dispersion in the spinal subarachnoid space. Appl. Math. Model 94, 516–533.

Kalata W, Martin BA, Oshinski JN, Jerosch-Herold M, Royston TJ & Loth F 2009 MR measurement of cerebrospinal fluid velocity wave speed in the spinal canal. IEEE Trans. Biomed 56 (6), 1765–1768.

Khani M, Sass LR, Xing T, Keith Sharp M, Balédent O & Martin BA 2018 Anthropomorphic model of intrathecal cerebrospinal fluid dynamics within the spinal subarachnoid space: spinal cord nerve roots increase steady-streaming. Trans. ASME J. Biomech. Engng 140 (8), 0810121–08101215.

Kurtcuoglu V, Jain K & Martin BA 2019 Modelling of cerebrospinal fluid flow by computational fluid dynamics. In Biomechanics of the Brain, pp. 215–241. Springer.

Lawrence JJ, Coenen W, Sánchez AL, Pawlak G, Martínez-Bazán C, Haughton V & Lasheras JC 2019 On the dispersion of a drug delivered intrathecally in the spinal canal. J. Fluid Mech 861, 679–720.

Linninger AA, Tangen K, Hsu C-Y & Frim D 2016 Cerebrospinal fluid mechanics and its coupling to cerebrovascular dynamics. nnu. Rev. Fluid Mech 48, 219–257.

Mortazavi MM et al. 2018 Subarachnoid trabeculae: a comprehensive review of their embryology, histology, morphology, and surgical significance. World Neurosurg. 111, 279–290. [PubMed: 29269062]

Ommaya AK 1968 Mechanical properties of tissues of the nervous system. J. Biomech 1 (2), 127–138. [PubMed: 16329300]

Sánchez AL, Martínez-Bazan C, Gutiérrez-Montes C, Criado-Hidalgo E, Pawlak G, Bradley W, Haughton V & Lasheras JC 2018 On the bulk motion of the cerebrospinal fluid in the spinal canal. J. Fluid Mech 841, 203–227.

Sincomb SJ, Coenen W, Criado-Hidalgo E, Wei K, King K, Borzage M, Haughton V, Sánchez AL & Lasheras JC 2021 Transmantle pressure computed from mr imaging measurements of aqueduct flow and dimensions. AJNR Am. J. Neuroradiol 42 (10), 1815–1821. [PubMed: 34385144]

Sincomb S, Coenen W, Sánchez AL & Lasheras JC 2020 A model for the oscillatory flow in the cerebral aqueduct. J. Fluid Mech 899, R1.

Singh V & Cheng R 2021 Neurovascular physiology and neurocritical care. In Handbook of Clinical Neurology, vol. 176, pp. 71–80. Elsevier. [PubMed: 33272411]

Stockman HW 2006 Effect of anatomical fine structure on the flow of cerebrospinal fluid in the spinal subarachnoid space. Trans. ASME J. Biomech. Engng 128 (1), 106–114.

Tada Y & Nagashima T 1994 Modeling and simulation of brain lesions by the finite-element method. IEEE Engng Med. Biol. Mag 13 (4), 497–503.

Tangen KM, Hsu Y, Zhu DC & Linninger AA 2015 CNS wide simulation of flow resistance and drug transport due to spinal microanatomy. J. Biomech 48 (10), 2144–2154. [PubMed: 25888012]

Thomas JH 2019 Fluid dynamics of cerebrospinal fluid flow in perivascular spaces. J. R. Soc. Interface 16 (159), 20190572. [PubMed: 31640500]

Unnerbäck M, Ottesen JT & Reinstrup P 2018 ICP curve morphology and intracranial flow-volume changes: a simultaneous ICP and cine phase contrast MRI study in humans. Acta Neurochir. 160 (2), 219–224. [PubMed: 29273948]

Wagshul ME, Chen JJ, Egnor MR, McCormack EJ & Roche PE 2006 Amplitude and phase of cerebrospinal fluid pulsations: experimental studies and review of the literature. J. Neurosurg 104 (5), 810–819. [PubMed: 16703889]

Wagshul ME, Eide PK & Madsen JR 2011 The pulsating brain: a review of experimental and clinical studies of intracranial pulsatility. Fluids Barriers CNS 8 (1), 5. [PubMed: 21349153]

Yallapragada N & Alperin N 2004 Characterization of spinal canal hydrodynamics and compliance using bond graph technique and CSF flow measurements by MRI. Proc. Intl Soc. Magn. Reson. Med 11, 2658.

Author Manuscript Author Manuscript Author Manuscript Author Manuscript

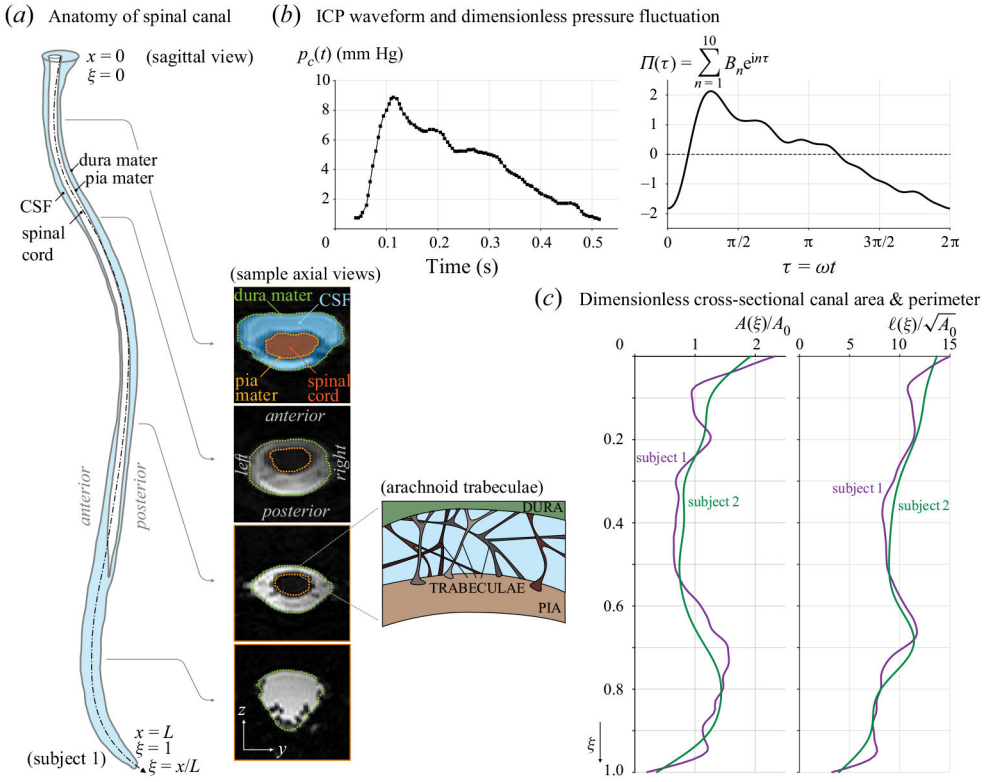

Figure 1.

(*a*) Main anatomical features of the spinal canal for subject 1; (*b*) ICP wave form (Wagshul, Eide & Madsen 2011) CC BY 2.0 (left subpanel) and dimensionless (right subpanel); (*c*) dimensionless canal functions for subjects 1 and 2.

Author Manuscript Author Manuscript Author Manuscript Author Manuscript

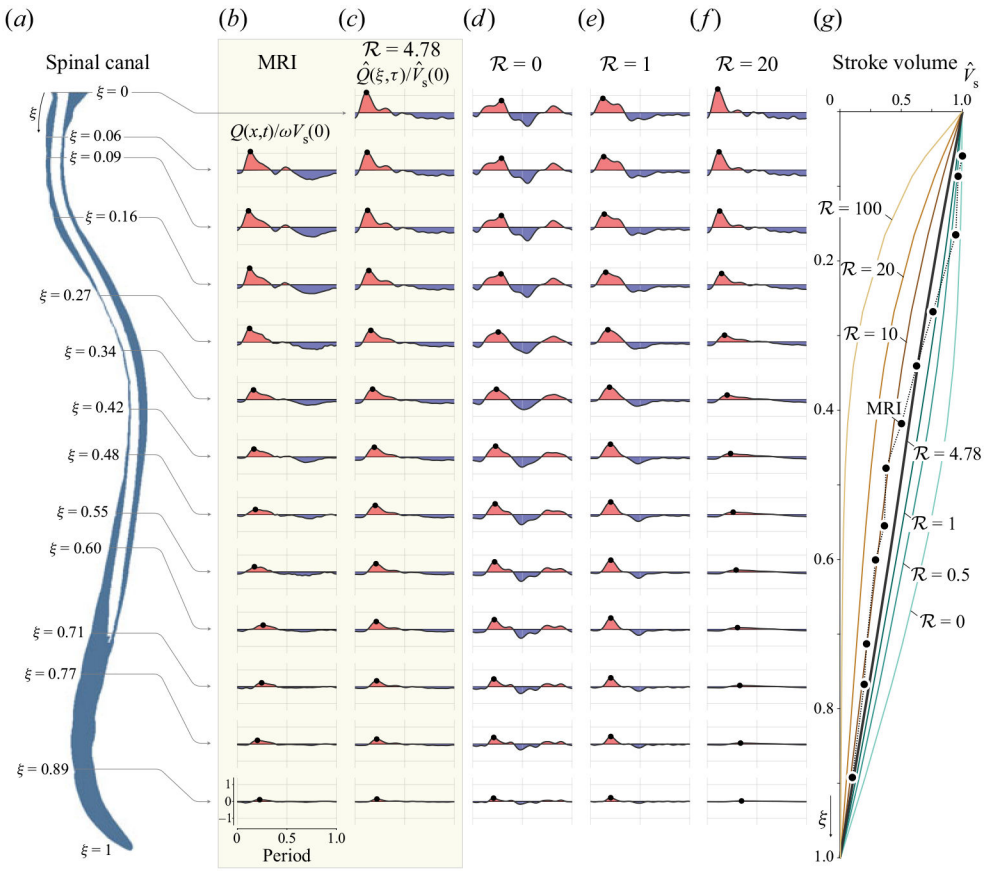

Figure 2.

Subject 1: selected spinal cord locations (*a*) with corresponding flow rate variation obtained from PC-MRI measurements (*b*) and from model predictions for $R = 4.78$ (*c*), $R = 0$ (*d*), $R = 1$ (*e*) and $R = 20$ (*f*), with associated normalized stroke volumes shown in (*g*).

Author Manuscript Author Manuscript Author Manuscript Author Manuscript

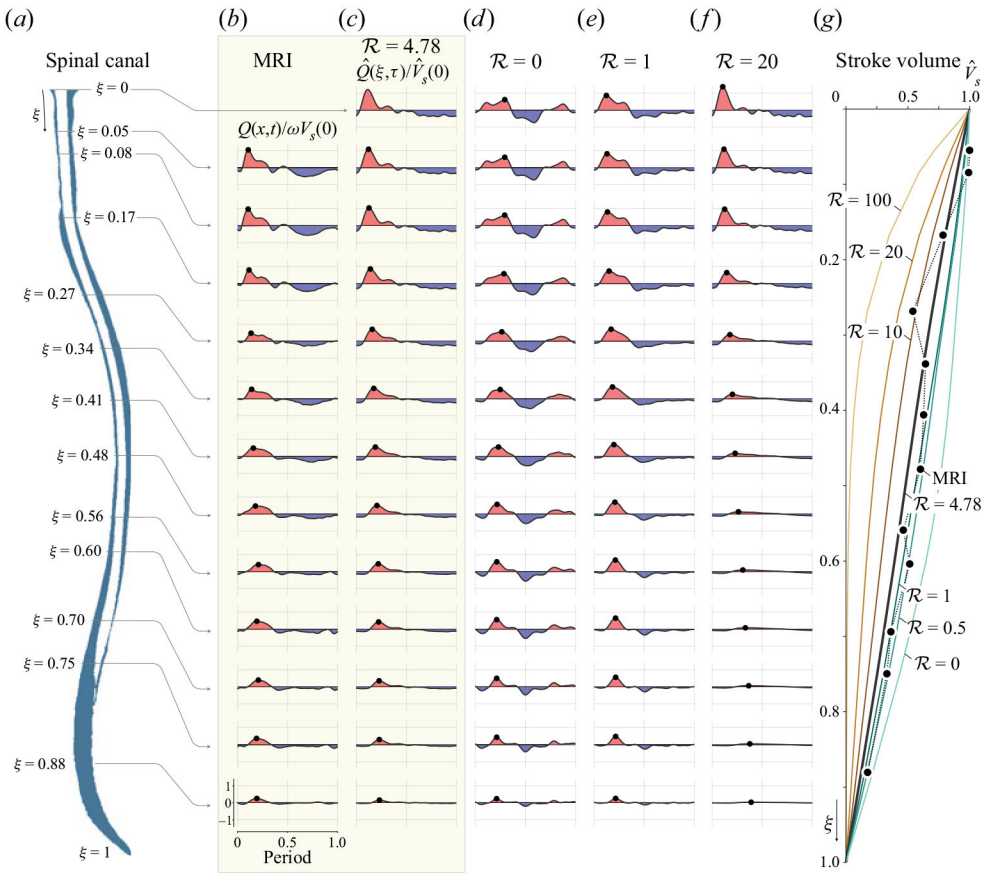

Figure 3.

Subject 2: selected spinal cord locations (*a*) with corresponding flow rate variation obtained from PC-MRI measurements (*b*) and from model predictions for $R = 4.78$ (*c*), $R = 0$ (*d*), $R = 1$ (*e*) and $R = 20$ (*f*), with associated normalized stroke volumes shown in (*g*).